

See discussions, stats, and author profiles for this publication at: <https://www.researchgate.net/publication/26837440>

Headgroup Effects on the Unusual Lamellar –Lamellar Coexistence and Vesicle-to-Micelle Transition of Salt-Free Catanionic Amphiphiles

ARTICLE in LANGMUIR · SEPTEMBER 2009

Impact Factor: 4.46 · DOI: 10.1021/la902963k · Source: PubMed

CITATIONS

18

READS

17

4 AUTHORS, INCLUDING:



Bruno F B Silva

International Iberian Nanotechnology Labor...

24 PUBLICATIONS 249 CITATIONS

SEE PROFILE



Ulf Olsson

Lund University

269 PUBLICATIONS 7,044 CITATIONS

SEE PROFILE



Ramon Pons

Institute of Advanced Chemistry of Cataloni...

101 PUBLICATIONS 1,368 CITATIONS

SEE PROFILE

Headgroup Effects on the Unusual Lamellar–Lamellar Coexistence and Vesicle-to-Micelle Transition of Salt-Free Catanionic Amphiphiles

Bruno F. B. Silva,[†] Eduardo F. Marques,^{*,†} Ulf Olsson,[‡] and Ramon Pons[§]

[†]*Centro de Investigação em Química, Department of Chemistry, Faculty of Science, University of Porto, Rua do Campo Alegre, n.º 687, P 4169-007 Porto, Portugal,* [‡]*Physical Chemistry, Centre for Chemistry and Chemical Engineering, Lund University, P.O. Box 124, SE-221 00 Lund, Sweden,* and [§]*Departament de Tecnologia Química i de Tensioactius, Institut de Química Avançada de Catalunya (IQAC), CSIC, Jordi Girona 18-26, E-08034 Barcelona, Spain*

Received August 10, 2009. Revised Manuscript Received September 2, 2009

Salt-free ion-paired catanionic amphiphiles of the $C_m^+ C_n^-$ type, with a high solubility mismatch ($n \gg m$ or $m \gg n$) display a remarkable phase behavior in water. A temperature-driven vesicle-to-micelle transition in the dilute side together with a coexistence of two lamellar phases on the concentrated side is one of the peculiar effects that have been reported for the hexadecyltrimethylammonium octylsulfonate surfactant, $C_{16}C_8$ or $TA_{16}So_8$ (extensive to $C_{14}C_8$ and $C_{12}C_8$). In this work, with $TA_{16}So_8$ as a reference, the cationic trimethylammonium (TA^+) and pyridinium (P^+) headgroups are combined with the anionic sulfate (S^-) and sulfonate (So^-) headgroups to yield other $C_{16}C_8$ compounds: hexadecyltrimethylammonium octylsulfate ($TA_{16}S_8$), 1-hexadecylpyridinium octylsulfonate ($P_{16}So_8$), and 1-hexadecylpyridinium octylsulfate ($P_{16}S_8$). We show that, if the asymmetry of the chain lengths is kept constant at $C_{16}C_8$ and the headgroup chemistry is changed, most of the unusual self-assembly properties are still observed, indicating that they are not system-specific but extensive to other combinations of headgroups and mainly dictated by the ion-pair solubility mismatch. Thus, all the compounds in water quite remarkably show a lamellar–lamellar phase coexistence and spontaneously form vesicles upon solubilization. Moreover, $P_{16}So_8$ undergoes a temperature-driven vesicle-to-micelle transition that involves an intermediate planar lamellar state, similar to $TA_{16}So_8$.

Some interesting effects on the global phase behavior, however, do arise when the headgroups are changed. Geometric packing effects are shown to be important, but the differences in phase behavior seem to be mainly dictated by (i) the charge density of the headgroups, which tunes the solubility mismatch of the ion-pair, and (ii) specific interactions between headgroups, which affect the short-range repulsive force that controls the swelling of the concentrated lamellar phase.

1. Introduction

Catanionic surfactants, or ion-paired amphiphiles, are complex salts of the type $C_m^+ C_n^-$ resulting from equimolar mixtures of a cationic, $C_m^+ X^-$, and an anionic, $C_n^- X^+$, amphiphile. Catanionic mixtures, in general, can be thought of as catanionic surfactants in the presence of inorganic salt ($X^+ X^-$) and excess ionic amphiphile, having been extensively studied for a couple of decades now.^{1–3} These mixtures have been found to possess an enormous variety of aggregate morphologies and strong synergism in interfacial properties, depending on a number of intensive variables (mainly concentration and mixing ratio). Spontaneously formed vesicles with long-term stability,^{4–11} wormlike and connected micelles often

with remarkable rheological properties,^{12–14} curious faceted structures,^{15,16} and intricate equilibria between liquid-crystalline phases^{17,18} are just some of the features that have attracted great interest over the years.

Such mixtures, however, are relatively complex because thermodynamically they are four-component systems, meaning that a complete investigation of their phase behavior would require the explicit addition of salt and, consequently, a prismatic or pyramidal diagram representation.^{17,19} If salt is totally removed from the mixture and the stoichiometry fixed to 1:1, though, simple binary surfactant–water systems are at hand and to a great extent these systems are easier to study experimentally, interpret, and model, while at the same time, other fascinating properties still emerge.^{20–26} In addition, the anhydrous surfactants per se have been found to possess a complex stepwise melting phase

*Corresponding author. E-mail: efmarque@fc.up.pt.

- (1) Tondre, C.; Cailliet, C. *Adv. Colloid Interface Sci.* **2001**, *93*, 115–134.
- (2) Marques, E. F.; Regev, O.; Khan, A.; Lindman, B. *Adv. Colloid Interface Sci.* **2003**, *100–102*, 83–104.
- (3) Šegota, S.; Težak, D. *Adv. Colloid Interface Sci.* **2006**, *121*, 51–75.
- (4) Kaler, E. W.; Herrington, K. L.; Murthy, A. K.; Zasadzinski, J. A. *J. Phys. Chem.* **1992**, *96*, 6698–6707.
- (5) Jung, H. T.; Coldren, B.; Zasadzinski, J. A.; Iampietro, D. J.; Kaler, E. W. *Proc. Natl. Acad. Sci. U.S.A.* **2001**, *98*, 1353.
- (6) Marques, E. F. *Langmuir* **2000**, *16*, 4798–4807.
- (7) Hao, J.; Yuan, Z.; Liu, W.; Hoffmann, H. J. *Phys. Chem. B* **2004**, *108*, 5105–5112.
- (8) Wang, Y. J.; Bai, G. Y.; Marques, E. F.; Yan, H. K. *J. Phys. Chem. B* **2006**, *110*, 5294–5300.
- (9) Brito, R. O.; Marques, E. F.; Gomes, P.; Falcão, S.; Söderman, O. *J. Phys. Chem. B* **2006**, *110*, 18158–18165.
- (10) Marques, E. F.; Brito, R. O.; Silva, S. G.; Rodriguez-Borges, J. E.; do Vale, M. L.; Gomes, P.; Araujo, M. J.; Soderman, O. *Langmuir* **2008**, *24*, 11009–11017.
- (11) Kakehashi, R.; Karlsson, G.; Almgren, M. *J. Colloid Interface Sci.* **2009**, *331*, 484–493.
- (12) Raghavan, S. R.; Fritz, G.; Kaler, E. W. *Langmuir* **2002**, *18*, 3797–3803.

- (13) Yousry, M.; Coppola, L.; Marques, E. F.; Nicotera, I. *J. Colloid Interface Sci.* **2008**, *324*, 192–198.
- (14) Abecassis, B.; Testard, F.; Zemb, T. *Soft Matter* **2009**, *5*, 974–978.
- (15) Meister, A.; Dubois, M.; Belloni, L.; Zemb, T. *Langmuir* **2003**, *19*, 7259–7263.
- (16) Antunes, F. E.; Brito, R. O.; Marques, E. F.; Lindman, B.; Miguel, M. *J. Phys. Chem. B* **2007**, *111*, 116–123.
- (17) Lindman, B.; Khan, A.; Marques, E.; Miguel, M. G.; Piculell, L.; Thalberg, K. *Pure Appl. Chem.* **1993**, *65*, 953.
- (18) Caria, A.; Khan, A. *Langmuir* **1996**, *12*, 6282–6290.
- (19) Thalberg, K.; Lindman, B.; Karlström, G. *J. Phys. Chem.* **1991**, *95*, 6004–6011.
- (20) Dubois, M.; Demé, B.; Gulik-Kryzwicki, T.; Dedeiu, J.-C.; Vautrin, C.; Désert, S.; Perez, E.; Zemb, T. *Nature* **2001**, *411*, 672–675.
- (21) Hao, J. C.; Liu, W. M.; Xu, G. Y.; Zheng, L. Q. *Langmuir* **2003**, *19*, 10635–10640.
- (22) Maurer, E.; Belloni, L.; Zemb, T.; Carrière, D. *Langmuir* **2007**, *23*, 6554.

behavior, with several thermotropic soft-crystal and liquid-crystalline phases as a function of temperature.^{27–29}

With respect to their aqueous phase behavior, most of the salt-free catanionic amphiphiles studied so far, bearing identical ($m = n$) or similar chain lengths ($|m - n| \leq 4$) with more than 10 carbons ($m, n \geq 10$), have been shown to be highly insoluble, to have relatively high gel-to-liquid crystal transition temperatures, and to generally form highly concentrated lamellar phases with limited swelling (*collapsed* phases), as demonstrated by the works of Jokela et al.^{30,31}

The picture is considerably different if the chain lengths are made asymmetric ($m \gg n$ or $m \ll n$) because two main factors now come into play. First, higher configurational entropy caused by the chain length mismatch is introduced in the crystalline lattice, leading to a relative destabilization of the crystal and to lower Krafft points. Second, because the shorter chain is more soluble than the longer chain, a net surface charge on the catanionic surfactant film arises. Both of these effects induce solubility into small aggregates, such as elongated micelles^{24,32–34} or vesicles.^{24,26,35–39} For instance, Eastoe et al.³² studied the micelles formed by a series of alkyltrimethylammonium dodecylsulfates, and for $m = 3–4$, the micelles were found to be cylindrical, whereas for $m = 6–7$, disk-shaped ones were formed. Several authors have shown that, in surfactant–hydrotrope systems (very similar to asymmetric catanionics), elongated micelles have a smaller charge density when the organic counterions are made hydrophobic (less soluble)³³ and that, upon increasing further this hydrophobicity, vesicles form instead of micelles.^{40,41}

At higher concentrations, the solubility mismatch can also give rise to curious phenomena, such as the striking formation of two lamellar phases in equilibrium, an extremely rare event in binary systems.²³ Persson et al.⁴² determined the temperature–composition phase diagram of a series of *N*-alkylpyridinium octylsulfonates, where m is varied between 0 and 8. In general, all the systems show an extended L_1 micellar region, but at higher surfactant volume fractions, liquid-crystalline phases are found, which strongly depend on m .

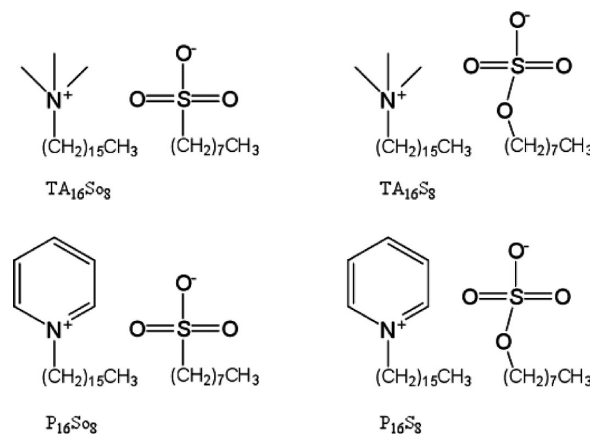


Figure 1. Molecular structure of the $C_{16}C_8$ salt-free ion-paired surfactants.

It can be expected that a higher solubility mismatch will increase the surfactant film charge density (σ), which will strengthen an electrostatic repulsive force (EI) and increase the spontaneous curvature (H_0) of the film. Therefore, an interesting interplay between aggregate shape (as dictated by H_0) and aggregate–aggregate interactions (through EI) can be expected when changing this parameter. These aspects have been investigated by us in detail for the surfactant hexadecyltrimethylammonium octylsulfonate (of the $C_{16}C_8$ type), both in the concentrated²³ and in the dilute region,²⁴ including the formation of microemulsions in the presence of decane.²⁵

However, the role of headgroup chemistry at a fixed chain length difference has not been addressed in a systematic way. In this work, three new $C_{16}C_8$ surfactants with different headgroups are prepared in an attempt to address two main questions. (i) Are the remarkable features of $TA_{16}S_8$ system-specific or can they be found in catanionic amphiphiles with other headgroups, once the chain mismatch is kept? (ii) Is the self-assembly and phase equilibria simply controlled by this solubility mismatch or do any changes appear, subtle or significant, owing to the headgroup chemistry influence? In this context, the cationic trimethylammonium (TA^+) and pyridinium (P^+) headgroups have been combined with the anionic sulfate (S^-) and sulfonate (So^-) headgroups to yield the following novel compounds: hexadecyltrimethylammonium octylsulfate ($TA_{16}S_8$), 1-hexadecylpyridinium octylsulfonate ($P_{16}S_8$), and 1-hexadecylpyridinium octylsulfate ($P_{16}S_8$). A multitechnique approach has been used, comprising calorimetric (DSC), optical (turbidity and light microscopy), interfacial (tensiometry), and scattering (SANS and SAXS) methods.

2. Experimental Section

2.1. Materials. Considering $TA_{16}S_8$ as the reference, three novel compounds of the $C_{16}^+C_8^-$ type (Figure 1) were prepared: hexadecylpyridinium octylsulfonate ($P_{16}S_8$), 1-hexadecylpyridinium octylsulfate ($P_{16}S_8$), and hexadecyltrimethylammonium octylsulfate ($TA_{16}S_8$). The surfactants hexadecyltrimethylammonium bromide (CTAB), *n*-hexadecylpyridinium chloride (CPC), sodium octylsulfonate (SOSO), all purchased from Sigma, and sodium octylsulfate (SOS), purchased from Fluka, were used as received for the preparation of the complex salts.

$TA_{16}S_8$ was available according to a preparation method previously reported.²³ $P_{16}S_8$, $P_{16}S_8$ and $TA_{16}S_8$ were prepared by mixing equimolar micellar solutions of the respective anionic and cationic surfactants with a slight excess of the short-chained one. The mixtures readily precipitate, and the crystalline solids

- (23) Silva, B. F. B.; Marques, E. F.; Olsson, U. *J. Phys. Chem. B* **2007**, *111*, 13520–13526.
- (24) Silva, B. F. B.; Marques, E. F.; Olsson, U. *Langmuir* **2008**, *24*, 10746–10754.
- (25) Silva, B. F. B.; Marques, E. F.; Olsson, U.; Linse, P. *J. Phys. Chem. B* **2009**, *113*, 10230–10239.
- (26) Yuan, Z. W.; Yin, Z. L.; Sun, S. X.; Hao, J. C. *J. Phys. Chem. B* **2008**, *112*, 1414–1419.
- (27) Tomašić, V.; Popović, S.; Filipović-Vinceković, N. *J. Colloid Interface Sci.* **1999**, *215*, 280–289.
- (28) Silva, B. F. B.; Marques, E. F. *J. Colloid Interface Sci.* **2005**, *290*, 267–274.
- (29) Marques, E. F.; Brito, R. O.; Wang, Y.; Silva, B. F. B. *J. Colloid Interface Sci.* **2006**, *294*, 240–247.
- (30) Jokela, P.; Jönsson, B.; Khan, A. *J. Phys. Chem.* **1987**, *91*, 3291–3298.
- (31) Jönsson, B.; Jokela, P.; Khan, A.; Lindman, B.; Sadaghiani, A. *Langmuir* **1991**, *7*, 889–895.
- (32) Eastoe, J.; Rogueda, P.; Shariatmadari, D.; Heenan, R. *Colloids Surf., A* **1996**, *117*, 215–225.
- (33) Oda, R.; Narayanan, J.; Hassan, P. A.; Manohar, C.; Salkar, R. A.; Kern, F.; Candau, S. *J. Langmuir* **1998**, *14*, 4364–4372.
- (34) Douliez, J. P.; Navailles, L.; Nallet, F. *Langmuir* **2006**, *22*, 622–627.
- (35) Aswal, V. K.; Haldar, J.; De, S.; Goyal, P. S.; Bhattacharya, S. *Phys. Chem. Chem. Phys.* **2003**, *5*, 907–910.
- (36) Vautrin, C.; Zemb, T.; Schneider, M.; Tanaka, M. *J. Phys. Chem. B* **2004**, *108*, 7986–7991.
- (37) Song, A.; Dong, S.; Jia, X.; Hao, J.; Liu, W.; Liu, T. *Angew. Chem., Int. Ed.* **2005**, *44*, 4018–4021.
- (38) Li, X.; Dong, S.; Jia, X.; Song, A.; Hao, J. *Chem.—Eur. J.* **2007**, *13*, 9495–9502.
- (39) Shen, Y. W.; Hao, J. C.; Hoffmann, H. *Soft Matter* **2007**, *3*, 1407–1412.
- (40) Hassan, P. A.; Narayanan, J.; Menon, S. V. G.; Salkar, R. A.; Samant, S. D.; Manohar, C. *Colloids Surf., A* **1996**, *117*, 89–94.
- (41) Buwalda, R. T.; Stuart, M. C. A.; Engberts, J. B. F. N. *Langmuir* **2000**, *16*, 6780–6786.
- (42) Persson, G.; Edlund, H.; Hedenström, E.; Lindblom, G. *Langmuir* **2004**, *20*, 1168–1179.

were copiously washed with water and vacuum-dried. The purity of the compounds was ascertained by elemental analysis. The absence of inorganic salt was further confirmed by sodium atomic emission and of that and other impurities by a polarizing microscopy and DSC study of the melting process of the solids. Furthermore, surface tension indicated no presence of surface-active organic impurities because no minima near the CMC was seen in the γ -log c plots.

2.2. Sample Preparation and Phase Diagram Determination.

The samples used in phase diagram mapping were all prepared by weighing surfactant and water, followed by vigorous mixing. Concentrated samples were further centrifuged upward and downward several times so that the composition was made homogeneous. The samples were then put in a thermostatted oven at the desired temperature and watched carefully until no changes were observed over a period of weeks to months. To facilitate the phase assignment, samples were inspected under crossed polarizers in search of birefringence. Selected samples were also examined with more quantitative techniques, such as DSC, SAXS, and SANS. The phase boundaries of $P_{16}S_{08}$ on the dilute side with increasing temperature were determined by turbidity heating scans and also confirmed by samples at rest in the oven.

2.3. Turbidity. Turbidity measurements were performed with an Agilent UV-vis spectrometer coupled with a thermostatted bath from Julabo. The heating/cooling rate was 1 K/min, and the used wavelength was 800 nm. The samples were measured in a 1 cm Hellma cell.

2.4. Differential Scanning Calorimetry (DSC). Heating-cooling-reheating scans were performed on a Setaram micro-DSCIII calorimeter. Aged samples and an equal amount of water (± 0.001 mg) were weighed in the measuring and reference cells, respectively. The standard cycle started with an isotherm of 1–4 h at 2 °C, to allow crystallization of the alkyl chains. This was especially critical in vesicle dispersions due to the slow crystallization kinetics. The heating/cooling rate was kept at 1 °C · min⁻¹.

2.5. Surface Tension. Surface tension measurements in dilute solutions were performed with a DCAT21 tensiometer from DataPhysics (Wilhelmy plate method).

2.6. Video-Enhanced and Polarized Light Microscopy (VEM and PLM). A polarizing light microscope, BX51 from Olympus, with differential interference contrast lenses, was used for phase assignment and visualization of aggregates. Images were acquired with an Olympus DP71 digital camera. Dilute samples were observed in sealed 0.2 mm-thick capillaries that allowed visualization up to 90 °C.

2.7. Small-Angle X-ray Scattering (SAXS). SAXS data were collected by a S3-MICRO (Hecus X-ray systems GMBH Graz, Austria) coupled to a GENIX-Fox 3D X-ray source (Xenocs, Grenoble), which provides a detector focused X-ray beam with $\lambda = 0.1542$ nm Cu K α line with more than 97% purity and less than 0.3% K α . Transmitted scattering was detected using a PSD 50 Hecus. The temperature was controlled by means of a Peltier TCCS-3 Hecus. Samples were inserted between two Mylar sheets with a 1 mm separation. The q values with this setup ranged from 0.08 to 6.0 nm⁻¹.

For a lamellar phase, the repeat distance d is obtained from the first Bragg peak according to

$$d = \frac{2\pi}{q} \quad (1)$$

The corresponding bilayer thickness δ can be obtained from eq 2

$$\delta = \Phi d \quad (2)$$

where Φ stands for surfactant volume fraction.

Table 1. Krafft Temperatures, T_{Kf} , for the Catanionic Compounds^a and Their CMC at 35 °C

compound	$T_{Kf}/^{\circ}\text{C}$	CMC/mmol · kg ⁻¹
TA ₁₆ SO ₈	15.9	0.088
TA ₁₆ S ₈	26.7	0.026
P ₁₆ SO ₈	33.0	0.054
P ₁₆ S ₈	26.1	0.024

^aBecause crystallization of bilayer alkyl chains in vesicles has a complex kinetic behavior, an evaluation of the transitions enthalpies changes has not been carried out. The Krafft temperatures were determined for 0.5 wt % samples and remain constant at least up to 1.5 wt %.

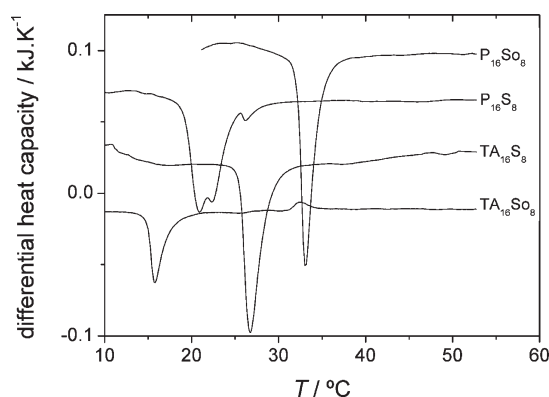


Figure 2. DSC thermograms for 0.5 wt % surfactant samples, where the endothermic peak signals the Krafft temperature of each compound. For $P_{16}S_8$, crystal dissolution is associated only with the third peak of the complex transition. For clarity, the curves were displaced vertically.

2.8. Small-Angle Neutron Scattering (SANS). The measurements were run in the SANS2 instrument⁴³ at SINQ lab in Paul Scherrer Institute (PSI), Switzerland. A range of scattering vectors q from 0.04 to 2.0 nm⁻¹ were covered by a combination of two wavelengths λ and three sample-to-detector distances SDD in three different experimental setups (set 1, $\lambda = 0.6$ nm, SDD = 1.2 m; set 2, $\lambda = 0.6$ nm, SDD = 3 m; set 3, $\lambda = 1.06$ nm, SDD = 6 m). The wavelength resolution was 10%. A detector with 128 × 128 pixels and a pixel size of 0.44 cm was used. The samples were kept in 2 mm quartz cells (Hellma). The two-dimensional isotropic scattering spectra have been corrected for detector efficiency by dividing the scattering spectra from the samples by the incoherent scattering spectra of neat water and subsequently has been radially averaged and converted to absolute scale. These steps were performed using the BerSANS software.⁴⁴ Background has then been subtracted, by subtracting the constant value of the incoherent scattering measured at high q values.

3. Results

3.1. Solubility and Critical Micelle Concentrations. At room temperature (25 °C), dilute and concentrated samples of TA₁₆S₈, P₁₆S₈, and P₁₆SO₈ all display a milky-like appearance due to a dispersion of the hydrated crystals in water, which sediment after some hours. By increasing the temperature, the P₁₆S₈ and TA₁₆S₈ samples acquire a bluish appearance in the dilute side (< 2 wt %), slightly above 26 °C, whereas they remain milky on the concentrated side. The same phenomena occur for P₁₆SO₈, but above 35 °C. Hence, in comparison with TA₁₆SO₈, the other catanionics show much higher Krafft temperatures (Table 1), as determined more quantitatively from the endothermic peaks in the DSC thermograms of Figure 2 (for 0.5 wt % dispersions).

(43) Strunz, P.; Mortensen, K.; Janssen, S. *Physica B* **2004**, *350*, e783–e786.

(44) Keiderling, U. *Appl. Phys. A: Mater. Sci. Process.* **2002**, *74*, S1455–S1457.

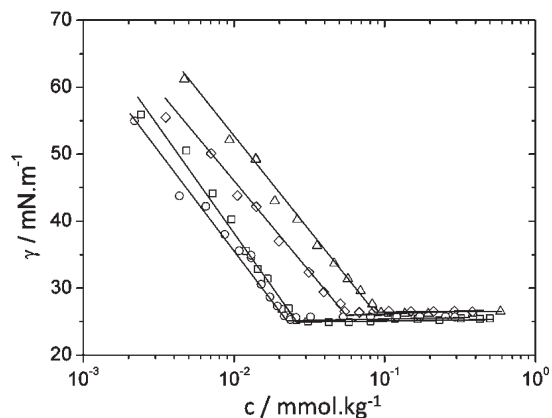


Figure 3. Surface tension measurements for the different catanionic compounds at 35 °C: TA₁₆S₈ (triangles), P₁₆S₈ (diamonds), TA₁₆S₈ (squares), and P₁₆S₈ (circles). The compounds having the sulfonate amphiphile have higher CMCs than the ones bearing sulfate. The surfactants bearing TA⁺ also have a slightly higher CMC.

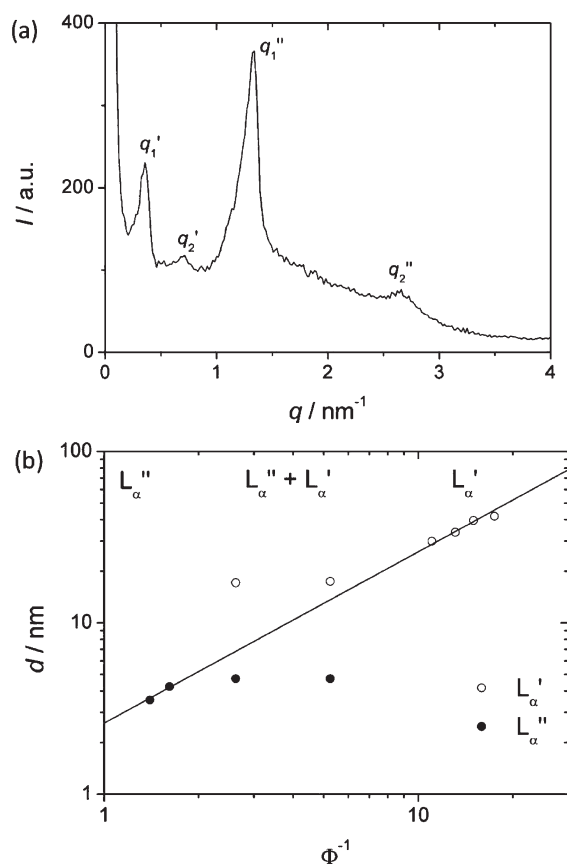


Figure 4. (a) SAXS diffractogram for P₁₆S₈ 20 wt % (in the miscibility gap). The first and second order Bragg peaks for both lamellar phases are clearly seen. (b) Swelling curve for the P₁₆S₈–water system (40 °C). The miscibility gap manifests itself with constant d spacing for both phases. From the slope (similar in both phases), the thickness obtained is $\delta = 2.6$ nm.

In the case of P₁₆S₈, the complex multipeak process appears to involve transitions between different hydrated crystalline states, with only the small peak at 26 °C corresponding to full solid dissolution, as checked by ocular and PLM observations.

With respect to the CMC values, determined by surface tension at 35 °C (Figure 3 and Table 1), the compounds bearing the

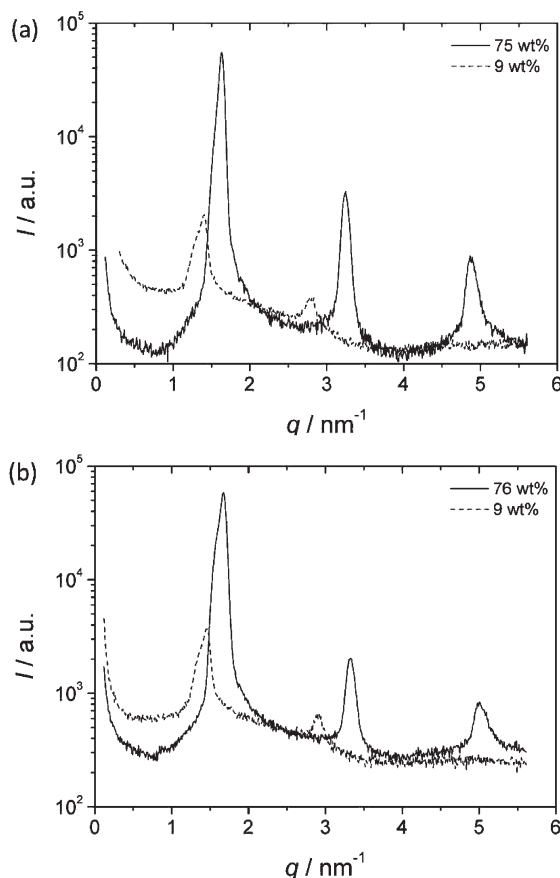


Figure 5. (a) TA₁₆S₈ and (b) P₁₆S₈ SAXS diffractograms. The 9 wt % samples are biphasic, and the Bragg peaks correspond to the collapsed L_α''. Assuming that the density is 1 for both compounds, the bilayer thickness is 2.9 nm for both. From the two-phase samples, the lower limit of L_α' is 64.5 wt % for TA₁₆S₈ and 66.3 wt % for P₁₆S₈.

sulfonate headgroup (TA₁₆S₈ and P₁₆S₈) show great similarities between them, as is the case with the sulfate ones (TA₁₆S₈ and P₁₆S₈). The general trend is that higher CMCs occur for the sulfonates, whereas for the same anionic headgroup, the CMC is higher for the trimethylammonium salts.

3.2. Concentrated Side. As with the TA₁₆S₈–water system, the concentrated side of these novel analogous catanionics is dominated by the coexistence of two lamellar phases, that is, a lamellar miscibility gap. Strikingly, aside from the much higher solubilization temperatures, the limits of the P₁₆S₈ miscibility gap are practically identical to those of TA₁₆S₈. This can be seen by direct visualization of prepared samples, in which the single lamellar phase samples are bluish and birefringent, and the two-phase samples are milky.

SAXS data clearly confirm these observations and more quantitatively. In Figure 4a, a sample from the two-phase region (20 wt %) shows the Bragg peaks corresponding to the coexisting lamellar spacings. Figure 4b shows the swelling curve of the P₁₆S₈–water system, evidencing the linear swelling behavior and the identical bilayer thickness of both lamellar phases. In the two-phase region, as expected, the spacings do not shift with composition. This figure is plotted as d versus Φ^{-1} . To calculate the volume fraction Φ from the wt % value, the density of P₁₆S₈ has been taken as 1.05 g cm^{−3} because visual observations show that it lies between that of normal and heavy water. From the slope of d versus Φ^{-1} , the thickness δ of the bilayer is found to be 2.6 nm. From this value and the two spacings of the biphasic sample, the miscibility gap limits are calculated as 16 and 58 wt %.

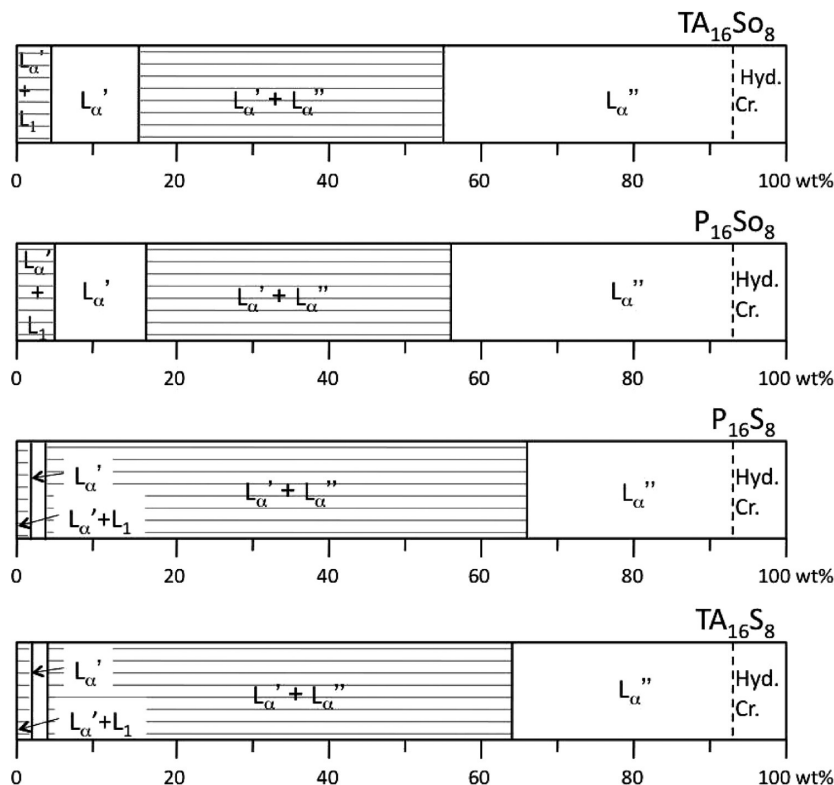


Figure 6. Phase diagrams for $P_{16}S_8$ –, $P_{16}S_8$ –, and $TA_{16}S_8$ –water systems at 40 °C and $TA_{16}S_8$ –water at 25 °C. Legend: L_1 , micellar solution phase; L_{α}' , swollen lamellar liquid-crystalline phase; L_{α}'' , collapsed lamellar liquid-crystalline phase; hyd. cr., hydrated crystals.

$P_{16}S_8$ and $TA_{16}S_8$ show a much more extended two-phase region. In Figure 5, one can see the SAXS curves for $TA_{16}S_8$ and $P_{16}S_8$ in the collapsed L_{α}'' and in the miscibility gap regions. The lamellar periodicity in all the samples is clear. If the density of both compounds is taken as 1, one obtains the value of 2.9 nm for the bilayer thickness in both compounds. From the lamellar repeat distance in the two-phase samples, the L_{α}'' lower limit is calculated as 65 wt % for $TA_{16}S_8$ and 66 wt % for $P_{16}S_8$, in good agreement with the observation of aged samples. In the range of 3.5–4 wt %, the samples shift from a milky appearance to bluish birefringent, suggesting that the L_{α}' becomes a single phase in this region. The Bragg reflections for these dilute phases are close to the lower limit of the experimental q -range and have a very weak intensity so as to be detected, but the observation of bilayer fragments and lamellar textures at higher dilutions supports the assignment of this region to a L_{α}' phase. The limit of this phase is thus set at 4 wt % for both compounds.

The phase diagrams for $P_{16}S_8$, $P_{16}S_8$ and $TA_{16}S_8$ in the concentrated side are presented in Figure 6.

3.3. Dilute Side. **3.3.1. Vesicle Formation for $TA_{16}S_8$ and $P_{16}S_8$.** At concentrations below 1.5 wt %, $TA_{16}S_8$ and $P_{16}S_8$ samples are bluish and display dynamic birefringence, indicating that the L_{α}' phase is no longer stable and is now dispersed in an isotropic L_1 phase along a two-phase region.

Light microscopy confirms that these bluish dispersions contain self-assembled, polydisperse giant vesicles (Figure 7a–e). We also note that these vesicles appear spontaneously, without shearing forces. Indeed, previously frozen $P_{16}S_8$ and $TA_{16}S_8$ samples spontaneously solubilize into the vesicles observed in Figure 7 when the temperature reaches 26 °C. In Figure 7a, solid crystallites of $TA_{16}S_8$ can be observed before they melt into vesicles (Figure 7b). Furthermore, the bluish dispersions are not stable and, with time, they start to flocculate into birefringent

domains. Clearly, these vesicles are not thermodynamically stable, and the dispersed L_{α}' domains start to reform with time.

Looking more closely into the appearance of these aggregates, the vesicles obtained for $TA_{16}S_8$ and $P_{16}S_8$ are relatively large, and many are elongated along the axis of the capillary. This is probably an effect of the thermal motion of the solution inside the capillary. The big air bubbles inside the capillary upon heating increase their internal pressure and randomly propel the vesicle solution inside the test tube. The friction of this motion on the capillary walls causes these vesicles to deform into elongated shapes. It is interesting to note the apparently high elasticity and robustness of these vesicles, able to sustain the shear forces without breaking. In the $P_{16}S_8$ case, along with the elongated vesicles, microtubules are also seen, with a persistence length of 5–10 μm and a contour length of ca. 40–100 μm . These microtubules are probably cylindrical bilayers and seem to result from shear forces. Swollen lamellae are also observed for all temperatures, whereas vesicles are stable up to 90 °C.

3.3.2. Vesicle–Micelle Transition for $P_{16}S_8$: Evidence for Intermediate Planar Bilayers. As with $TA_{16}S_8$ and $P_{16}S_8$, $P_{16}S_8$ also forms vesicles spontaneously at concentrations lower than 2 wt %, when solid dispersions are heated above 35 °C. In contrast with these two compounds, though, and similar to $TA_{16}S_8$, $P_{16}S_8$ undergoes a transition to a clear, colorless, and viscous phase at higher temperatures, whereas $TA_{16}S_8$ and $P_{16}S_8$ do not. This can be captured in a more quantitative way with turbidity, as displayed in Figure 8a. In close similarity with $TA_{16}S_8$, there is an intermediate region where the turbidity increases abruptly before decaying to nearly zero.

With microscopy Figure 8b, it can be seen that, following the solid solubilization, a very concentrated volume-filling (probably vesicle) dispersion is seen in high thermal motion. In the turbidity increase region, a static rough texture develops before an isotropic

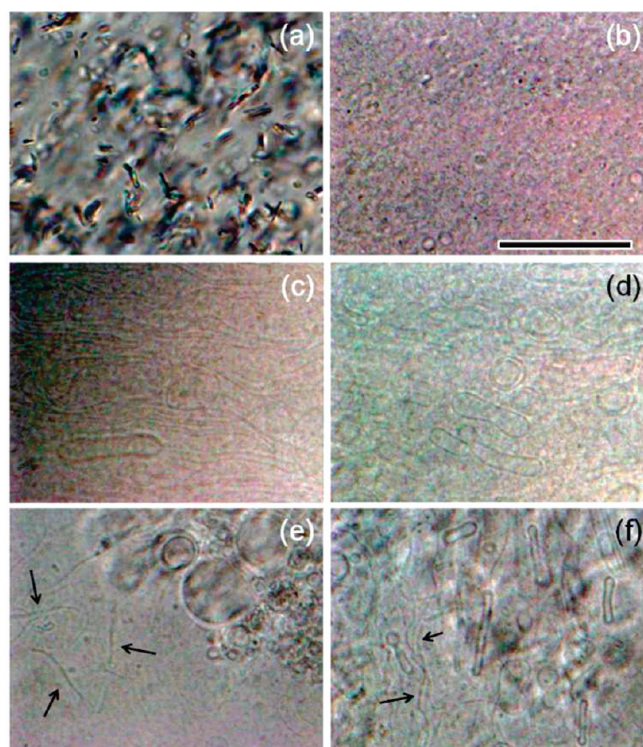


Figure 7. (a) TA₁₆S₈, 26 °C. Onset of vesicle formation from crystals. (b) TA₁₆S₈, 29 °C. Vesicles spontaneously formed from the crystals in (a). (c) TA₁₆S₈, 90 °C. Spherical and (mostly) elongated vesicles, aligned in the flow direction (horizontal). (d) TA₁₆S₈, 26 °C (cooling). Most of the vesicles are still elongated and stable, even at low temperatures, when the flow induced by heating is meaningless. (e) P₁₆S₈, 28 °C. After melting of the solid, three main aggregates are observed: swollen lamellae, with some myelinic figures; vesicles detaching from the lamellae; and probably bilayer tubules (black arrows) that look like fibers. These presumed tubules have a diameter smaller than 1 μm and a persistence length of 5–10 μm. (f) P₁₆S₈, 50 °C. Elongated vesicles aligned in the flow direction (vertical), coexisting with spherical vesicles, bilayer tubules, and lamellae. Scale bar: 50 μm (common to all the figures).

image is observed at even higher temperatures, corresponding to the (nearly) zero turbidity region. On cooling, the reverse transition is observed, as displayed in Figure 8c.

This puzzling vesicle/micelle transition for P₁₆S₈ was addressed with SANS. With this technique, one has a broader length range (in this case, 2–100 nm), as well as a better ensemble average. This is particularly useful to characterize the structure responsible for the rough texture and turbidity increase observed for P₁₆S₈ at higher temperatures, between the vesicle and L₁ phases.

At 40 °C, the scattering curve displays a flat q^{-2} dependence in Figure 9, in agreement with the polydisperse vesicles observed by microscopy. A very shallow dip is found at ca. 0.08 nm⁻¹, hampering a good size determination. At higher temperatures, slightly above the region where the rough texture is formed, a different scattering pattern is observed. At 75 °C, some slight changes are noticeable at low q values, whereas at 80 °C, superimposed with the q^{-2} dependence, two Bragg peaks at $q = 0.07$ nm⁻¹ and $q = 0.14$ nm⁻¹ appear, consistent with a lamellar phase with $d = 87$ nm. From the bilayer thickness ($\delta = 2.6$ nm), the composition of this phase is $\Phi = 0.03$.

It is, therefore, clear that the turbidity increase corresponds to the formation of a two-phase region, where the vesicles undergo fusion into a planar lamellar phase, an effect that has also been

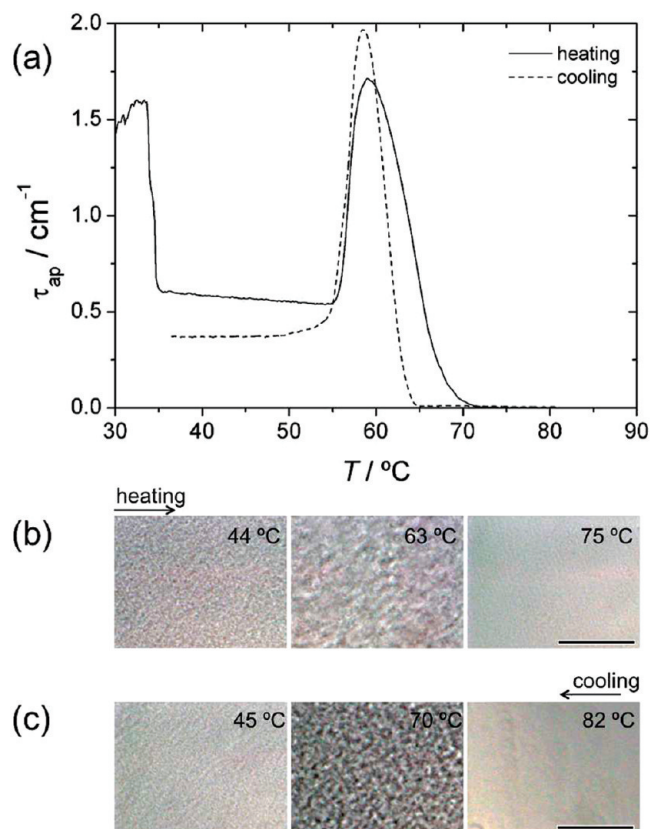


Figure 8. (a) Turbidity vs temperature scans of a 0.5 wt % P₁₆S₈ sample in D₂O. The initial high turbidity corresponds to the dispersed solid that solubilizes at 35 °C. Similar to TA₁₆S₈, P₁₆S₈ undergoes a transition to a colorless and viscous phase of almost zero turbidity, preceded by an intermediate regime, where turbidity increases. The transition is reversible. (b) Micrographs of a heating scan for a P₁₆S₈ 0.5 wt % sample. At 40 °C, what seems to be a highly concentrated dispersion of vesicles transforms into a static rough texture at 63 °C. At 75 °C, the sample becomes isotropic. (c) Micrographs of a P₁₆S₈ 1.6 wt % sample cooling scan. The scale bar is 50 μm.

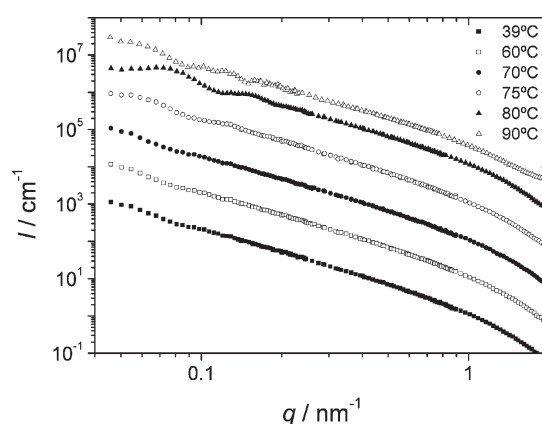


Figure 9. SANS results for the P₁₆S₈–D₂O system with increasing temperature. The intermediate vesicle–lamellae transition is visible at 80 °C through the appearance of the smooth peaks. Note that in D₂O, the phase boundaries shift to higher temperature.

seen for TA₁₆S₈. At 90 °C, the Bragg peaks disappear, but the q^{-2} power-law decay is still observed. This may indicate that, at 90 °C, the sample is still biphasic because microscopy indicates that the low-turbidity region is isotropic, consistent with an L₁

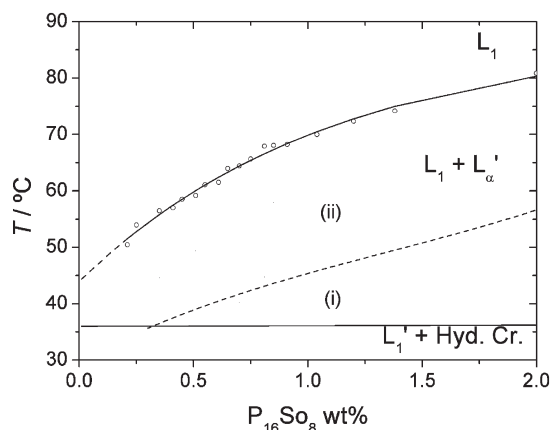


Figure 10. Phase diagram for the $P_{16}S_8$ –water system. L_1 and L_1' are isotropic phases. The former is probably constituted by elongated micelles (due to the viscosity). The $L_1 + L_{\alpha}'$ region is a two-phase region, where the lamellar phase L_{α}' is in the form of vesicles in region (i) and in the planar form in (ii).

phase. The high viscosity and clear, colorless appearance of the samples strongly suggest the presence of elongated micelles.

The global evaluation of the data previously presented enables the phase diagram (Φ vs T) of the $P_{16}S_8$ to be drawn (Figure 10). The phase boundaries are obtained mainly from turbidity data, which allows a good determination of the disconnected lamellar (vesicles)-to-connected lamellar (L_{α}') phase transition (having in mind that both belong to the two-phase $L_{\alpha}' + L_1$ region), as well as L_{α}' -to- L_1 transition. Microscopy and SANS are used to characterize the aggregates, whereas direct observation of the samples at rest is useful to check if the samples are in equilibrium. For most of these vesicle phases, some clouding was observed after some days at rest.

In the case of $P_{16}S_8$ and $TA_{16}S_8$, the vesicles formed are clearly metastable and, because no changes in phase behavior are detected when the temperature is changed (except for the solubilization temperature), the Φ versus T phase diagrams are not drawn.

4. Discussion

For the compounds studied here, the headgroup chemistry is changed while the chain length asymmetry is kept constant. Because of the solubility differences between the headgroups, the solubility mismatch is also affected. Additionally, some specific interactions between the headgroups also come into play. Furthermore, despite the much bigger molecular differences between the trimethylammonium (TA^+) and pyridinium (P^+) headgroups, it is the anionic group that has the main impact on the global phase behavior. In what follows, we will divide the discussion between the concentrated and the dilute region.

4.1. Concentrated Side: Interpretation and Modeling of the Lamellar Miscibility Gap. To start with, we briefly recall that the coexistence of two lamellar phases in the $TA_{16}S_8$ –water system has been interpreted and modeled in terms of an equation of state for the lamellar phase that bears additive contributions from an attractive force (van der Waals force, vdW) and two repulsive forces (electrostatic, El, and short-range, SRR, forces).^{23,25} The total osmotic pressure of the system, $\Pi_{\text{tot}} = \Pi_{\text{vdW}} + \Pi_{\text{El}} + \Pi_{\text{SRR}}$, could thus be plotted as a function of the interlamellar distance, L .

The magnitude of the El force is determined by the charge density of the catanionic bilayer, σ , which depends on the surfactant volume fraction, Φ , and the effective solubility of the

short-chain ion, $[C_8^-]_{\text{eff}}$, according to²⁵

$$\sigma = \frac{1}{2} [C_8^-]_{\text{eff}} \cdot \delta \cdot \left(\frac{1}{\Phi} - 1 \right) \quad (3)$$

where σ has the dimensions of number of unit charges per unit area and δ is the bilayer thickness. It is also worth bringing to mind that this effective solubility $[So^-]_{\text{eff}}$ is smaller than the intrinsic solubility $[So^-]_0$ (constant theoretical solubility of C_8^- in the absence of the electrostatic penalty derived from the bilayer charging-up), according to a proposed charge-regulation mechanism.²⁵ $[So^-]_{\text{eff}}$ decreases as the surfactant concentration is lowered, to partially compensate the increase in charge density.

With respect to the SRR force, we recall that, phenomenologically, this force decays exponentially with the interbilayer distance but at short distances is extremely high and usually dominant over all others.²³

For $TA_{16}S_8$, the two-phase region between the lamellar phases lies between 15 and 54 wt %. Quite remarkably, despite the different solubility temperature (likely caused by a stabilization of the solid phase induced by the planar P^+ headgroup), $P_{16}S_8$ has a very similar phase behavior, with the miscibility gap lying between 16 and 58 wt %. In contrast, the sulfate-bearing compounds $TA_{16}S_8$ and $P_{16}S_8$ have a much wider miscibility gap, with the collapsed L_{α}' lower limit situated at 65 and 66 wt % for $TA_{16}S_8$ and $P_{16}S_8$, respectively. The L_{α}' upper limit lies approximately at 4 wt %. Two factors seem to justify this trend.

Picking the lower limits of the collapsed L_{α}' phase, it can be seen that this phase has a higher stability range in the sulfonate (So^-) compounds. This suggests that the short-range repulsive (SRR) force is stronger, that is, more long-ranged in these compounds than in the sulfate ones. This effect is somewhat surprising because the big molecular differences between the cationic headgroups do not seem to influence the SRR potential but subtle differences on the anionic part do. Within the model, the weaker SRR force in sulfates, on its own, widens the miscibility gap.

Besides the influence of the SRR force—which affects the whole equation of state— L_{α}' is mainly controlled by the solubility mismatch because electrostatic repulsions arising from this effect can stabilize lamellar phases at higher dilutions. The sulfonate headgroup has a higher charge density than that of sulfate and thus should be slightly more soluble. The negative charge of sulfonate is distributed within three oxygen atoms, whereas in sulfate, it is distributed within four atoms, lowering the charge density. An additional indication of a higher solubility of So_8^- when compared with S_8^- comes from the CMC values of SOS and SOSo, with the later being slightly higher. This causes a slightly higher solubility mismatch and a higher surface charge density in the bilayers, providing additional stabilization. This effect per se is enough to increase the stability of the L_{α}' phase to higher concentrations in sulfonates compared to sulfates and thus decrease the width of the miscibility gap.

With the above-mentioned charge-regulation mechanism in mind, the phase behavior of $TA_{16}S_8$ and $P_{16}S_8$ can be modeled, assuming an intrinsic solubility for the most soluble part ($[S^-]_0$ for octylsulfate). In Figure 11 and Table 2, the results of these calculations are shown (for further details on the procedure, refs 23 and 25 should be consulted). A characteristic van der Waals loop is seen in the Π – L curve, signifying the coexistence of the two lamellar phases. The phase boundaries of this two-phase region can then be calculated through a Maxwell construction,⁴⁵

(45) Wennerström, H. *Langmuir* **1990**, *6*, 834–838.

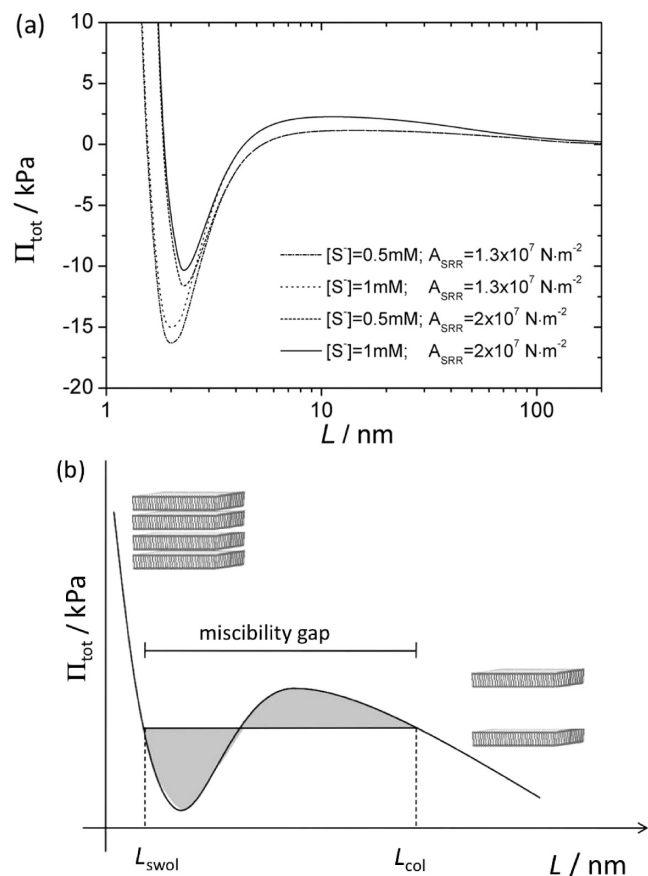


Figure 11. Model calculations for the lamellar miscibility gap. (a) Osmotic pressure vs interlamellar distance ($L = d - \delta$) for different values of octylsulfate intrinsic solubility ($[S^-]_0$) and of the SRR force amplitude (A_{SRR}). $\delta = 2.9 \text{ nm}$. The overall osmotic pressure Π_{total} is the sum of the van der Waals, short-range repulsive, and electrostatic forces in the catanionic bilayers. (b) Schematic representation displaying the Maxwell construction, whereby the van der Waals loop is divided into two halves of equal area, the shaded regions (adapted).⁴⁵ The limits of this region are the interlamellar spacing of the collapsed L_{col} and swollen L_{swol} phases.

illustrated in Figure 11b, for the sake of clarity, where the two shaded areas are made exactly equal.

The miscibility gap limits (4–65 wt % for TA_{16}S_8 and 4–66 wt % for P_{16}S_8) for both compounds are reasonably well-described with $[S^-]_0 = 0.5 \text{ mM}$ and $A_{\text{SRR}} = 1.33 \times 10^7 \text{ N} \cdot \text{m}^{-2}$ (a parameter describing the strength of the SRR force).²³ As can be seen in Table 2, the SRR force controls the lower limit of the collapsed lamellar phase ($L_{\alpha''}$) and has also a slight influence on the upper limit of the swollen phase ($L_{\alpha'}$). $[S^-]_0$ is related to the solubility mismatch and is the main contribution for $L_{\alpha'}$ phase stability. $[S^-]_0$ has a negligible effect on the stability of $L_{\alpha''}$ because the SRR pressure is very steep.

In the case of So^- , the miscibility gap is best fit with $A_{\text{SRR}} = 4.00 \times 10^7 \text{ N} \cdot \text{m}^{-2}$, which means that, in addition to the higher solubility ($[\text{So}^-]_0 = 2.5 \text{ mM}$), So^- also induces a stronger SRR force.²⁵ Therefore, specific effects of the anionic group seem to be also important for the global phase behavior description.

4.2. Dilute Side. The lower limit of $L_{\alpha'}$ is also controlled in part by the solubility mismatch. On one hand, high values of the mismatch strengthen the electrostatic stabilizing force, increasing the stability range of $L_{\alpha'}$. On the other hand, they also dampen possible undulations, decreasing the stability range at higher dilutions. Additionally, if the mismatch increases so much that

Table 2. Limits of the Miscibility Gap for the Modeled TA_{16}S_8 –Water and P_{16}S_8 –Water Systems

$[S^-]_0/\text{mM}$	$A_{\text{SRR}} \times 10^7/\text{N} \cdot \text{m}^{-2}$	$L_{\alpha'}$ upper limit/wt %	$L_{\alpha''}$ lower limit/wt %
0.5	2.00	4.0	62
	1.33	3.4	66
1.0	2.00	6.7	61
	1.33	5.7	66

it induces a change in H_0 , then other phases (such as vesicles or micelles) may become energetically more favorable than the planar lamellar phase. A combination of these two effects might be responsible for the more limited swelling obtained for TA_{16}S_8 and P_{16}S_8 (ca. 2.6 wt %) when compared to TA_{16}S_8 and P_{16}S_8 (ca. 1.5 wt %). Because the mismatch is lower in TA_{16}S_8 and P_{16}S_8 , these values do not change H_0 enough, and $L_{\alpha'}$ is kept until a lower limit.

In view of the higher solubility mismatch, both TA_{16}S_8 and P_{16}S_8 undergo a transition to an isotropic L_1 phase at higher temperatures, whereas TA_{16}S_8 and P_{16}S_8 do not. The nature of the L_1 phase was not fully investigated for P_{16}S_8 , but in analogy with TA_{16}S_8 and because the clear isotropic solutions are more viscous than the bluish ones, this phase is most likely composed of elongated micelles.²⁴

Also, in close resemblance with the TA_{16}S_8 compound, P_{16}S_8 undergoes an intermediate transition where vesicles are found to fuse into planar bilayers before the micellar L_1 phase is reached. In our view, this opens up the possibility that the vesicles observed at lower temperatures may be at thermodynamic equilibrium, but further investigations are needed on this issue before the nature of this remarkable transition becomes clear.

4.3. Overview. As a final comment, it has been seen that the nature of the anionic headgroup seems to determine the overall phase behavior to a much higher extent than the cationic one. This is striking because the molecular structures of So^- and S^- are very similar, only differing slightly on the headgroup charge density. In our view, this is, in part, explained by the fact that, here, the anionic group is clearly the most soluble one. Hence, minor solubility differences between the headgroups have a higher impact on the overall solubility mismatch, affecting the global phase behavior especially on the dilute side. The specific effects on the SRR force, manifested on the concentrated side, are less obvious mainly because (once again) of the very similar molecular structures between So^- and S^- . With this in mind, a more detailed investigation of headgroup effects on the SRR force could be useful to shed light into the physical nature of this still elusive force.⁴⁶

5. Concluding Remarks

In this paper, the influence of the nature of the ionic headgroup of some asymmetric catanionics on the aggregation behavior in water has been investigated. One finds that the charge density of the most soluble part affects the solubility mismatch and, consequently, the stability of the swollen lamellar phase ($L_{\alpha'}$). This stabilization arises from electrostatic forces originated by the higher mismatch. Higher charge density in the most soluble part greatly increases the upper stability limit of the $L_{\alpha'}$ phase, reducing the miscibility gap. In contrast, it reduces its lower limit at higher dilutions, inducing the formation of a solution phase. Moreover, the sulfonate headgroup induces a stronger SRR repulsive force when compared with the sulfate case. Both these effects promote a narrower miscibility gap in sulfonate-bearing compounds.

(46) Israelachvili, J.; Wennerström, H. *Nature* **1996**, 379, 219–225.

One can further conclude that the charge density of the less soluble part has a negligible effect on the phase behavior.

On the dilute side, P_{16}So_8 also has an interesting temperature-dependent phase behavior, similar to the $\text{TA}_{16}\text{So}_8$ case. At temperatures slightly higher than the solubilization temperature, polydisperse vesicles are found. Raising the temperature increases the solubility mismatch, inducing the formation of an isotropic phase. At intermediate temperatures, before the single L_1 phase is formed, vesicles undergo fusion into a planar lamellar phase.

Acknowledgment. We are grateful for financial support from the following institutions: Portuguese Science Foundation (FCT)

and FEDER Funds, through POCTI/QUI/44296/2002; Centro de Investigação em Química - linha 5; Spanish Ministry of Science and Innovation (CTQ2006-01582); Swedish Research Council (VR); and European Commission under the sixth FP through the Key Action: Strengthening the European Research Area, Research Infrastructures (Contract No. RII3-CT-2003-505925). B.F.B.S. is also grateful to FCT for the Ph.D. grant, SFRH/BD/24966/2005. Part of this work is based on experiments performed at the Swiss spallation neutron source SINQ, Paul Scherrer Institute, Villigen, Switzerland, where the help of our local contact, Urs Gasser, is gratefully acknowledged. J. Caelles from the SAXS-WAXS service at IQAC is acknowledged for performing the SAXS experiments.